Pathological evaluation of rats carrying in-frame mutations in the dystrophin gene: A new model of Becker muscular dystrophy

Authors

Naomi Teramoto[1], Hidetoshi Sugihara[1], Keitaro Yamanouchi[1], Katsuyuki Nakamura[1], Koichi Kimura[2, 3], Tomoko Okano[4], Takanori Shiga[5], Taku Shirakawa[6, 7], Masafumi Matsuo[6, 7], Tetsuya Nagata[8], Masao Daimon[4], Takashi Matsuwaki[1], Masugi Nishihara[1]

Author affiliations

1. Department of Veterinary Physiology, Graduate School of Agricultural and Life Sciences, The University of Tokyo, Bunkyo-ku, Tokyo, 113-8657, Japan

2. Department of General Medicine, The Institute of Medical Science, The University of Tokyo, Minato-ku, Tokyo, 108-8639, Japan

3. Department of Cardiovascular Medicine, Graduate School of Medicine, The University of Tokyo, Bunkyo-ku, Tokyo, 113-0033, Japan

4. Department of Laboratory Medicine, The University of Tokyo Hospital, The University of Tokyo, Bunkyo-ku, Tokyo, 113- 8655, Japan

5. Department of Veterinary Pathology, Graduate School of Agricultural and Life Sciences, The University of Tokyo, Bunkyo-ku, Tokyo, 113-8657, Japan

6. Research Center for Locomotion Biology, Kobe Gakuin University, Nishi, Kobe, 651-2180, Japan

7. KNC Department of Nucleic Acid Drug Discovery, Faculty of Rehabilitation, Kobe Gakuin University, Nishi, Kobe, 651-2180, Japan

8. Department of Neurology and Neurological Science, Tokyo Medical and Dental University, Bunkyo-ku, Tokyo 113-8510, Japan

Summary statement

The newly established rat model carrying in-frame mutations in the *Dmd* gene exhibits the dystrophic phenotype and abnormal dystrophin expression profile, similar to patients with Becker muscular dystrophy.

Abstract

Dystrophin, encoded by the *DMD* gene on the X chromosome, stabilizes the sarcolemma by linking the actin cytoskeleton with the dystrophin-glycoprotein complex (DGC). In-frame mutations in *DMD* cause a milder form of X-linked muscular dystrophy, called Becker muscular dystrophy (BMD), characterized by the reduced expression of truncated dystrophin. So far, no animal model with in-frame mutations in *Dmd* has been established. As a result, the effect of in-frame mutations on the dystrophin expression profile and disease progression of BMD remains unclear. In this study, we established a novel rat model carrying in-frame *Dmd* gene mutations (IF rats) and evaluated the pathology. We found that IF rats exhibit reduced expression of truncated dystrophin in a proteasome-independent manner. This abnormal dystrophin expression caused dystrophic changes in muscle tissues, but did not lead to functional deficiency. We also found that the expression of additional dystrophin named dpX, which forms the DGC in the sarcolemma, is associated with the appearance of truncated dystrophin. In conclusion, the outcomes of this study contribute to the further understanding of BMD pathology and help elucidate the efficiency of dystrophin recovery treatments in Duchenne muscular dystrophy, a more severe form of X-linked muscular dystrophy.

Introduction

Dystrophin (dp427), a 427 kDa protein crucial for sarcolemma integrity, is encoded by the dystrophin gene (*DMD* gene) on the X chromosome (Hoffman et al., 1987). Dystrophin functions as a sarcolemma-supporting protein during muscle contraction by linking the intracellular actin cytoskeleton to transmembrane components of the dystrophin-associated glycoprotein complex (DGC). The DGC is composed of several proteins represented by sarcoglycans, dystroglycans, and neuronal nitric oxide synthase (nNOS) (Lapidos et al., 2004). The function of dystrophin requires its N-terminal and C-terminal sequences, which are essential for binding with the cytoskeletal actin filament and with β-dystroglycan (βDG), respectively, in DGC (Campbell and Kahl, 1989; Rybakova et al., 1996). The central part of dystrophin is called the central rod domain, and is composed of 24 spectrin-like repeats (Koenig et al., 1988).

X-linked muscular dystrophy is a recessive genetic disease characterized by progressive muscle wasting. Becker muscular dystrophy (BMD) is a form of X-linked muscular dystrophy caused by in-frame mutations in *DMD*. In BMD muscle tissues, a truncated form of dystrophin (tdp427) is expressed, based on the missing genomic sequence. The pathology of this disease is generally milder than that of Duchenne muscular dystrophy (DMD), known as a more severe form of X-linked muscular dystrophy caused by the complete loss of the dystrophin protein. Patients with DMD show debilitating clinical symptoms, such as a difficulty in walking and standing, heart failure, and respiratory difficulties. In contrast, the clinical severity of BMD varies among individuals, from asymptomatic to as severe as DMD (Koenig et al., 1989).

Exon skipping is the latest therapeutic strategy for the conversion of DMD to BMD by skipping the mutated exons using antisense oligonucleotide (AON). Recently, the 10th AON drug was approved for use in clinical settings (Heo, 2020). In the near future, the

pathology of many patients with DMD is expected to become as mild as that of patients with BMD, owing to such therapeutic options. However, even the latest therapy can only alleviate the clinical symptoms by converting DMD to BMD, but a complete cure of DMD and BMD still warrants future research to analyze the disease progression.

In patients with BMD, expression levels of tdp427 and DGC components are lower and more varied than those in healthy controls, and the levels are variable within single myofibers, between adjacent myofibers, and between muscles (Beggs et al., 1991). Immunohistochemically, BMD muscle tissues show "faint and patchy" staining of dystrophin. There is a still conflict about the use of dystrophin as a surrogate biomarker: Anthony and colleagues reported the expression level of tdp427 in muscle tissues is well-correlated with the clinical severity of BMD, whereas Van Den Bergen and colleagues reported that tdp427 levels appear not to be a major determinant of disease severity in BMD, as long as it is above approximately 10%. (Anthony et al., 2011; Van Den Bergen et al., 2014). After all, although it is still under debate, more than 90% decrease of normal dystrophin levels may have a critical effect on the clinical severity of the patients with BMD. Previous studies examined the mechanisms underlying the decrease of tdp427, using *in vitro* analyses or transgenic mice that overexpress tdp427, and showed that the decreased level of tdp427 was caused by protein degradation following the tertiary instability of the protein (Henderson et al., 2011; McCourt et al., 2015; McCourt et al., 2018). However, since patients with BMD exhibit endogenous tdp427 expression under normal promoter activity, such an *in vitro* or over-expressed tdp427 scenario may not mimic the physiological environment in muscle tissues of patients with BMD. Nevertheless, so far, no animal models carrying the in-frame mutation in the *Dmd* gene and representing reduced endogenous expression of tdp427 have been reported.

Previously, our group generated dystrophin-mutated rat strains using CRISPR/Cas-mediated gene editing targeting in 5' region of *Dmd* gene (Nakamura et al., 2014). Several rat

strains completely lacked dystrophin protein owing to the out-of-frame mutation in *Dmd,* and have shown progressive pathology similar to human patients with DMD in their skeletal and cardiac muscles, unlike the widely used dystrophin-deficient mouse strain (mdx mice). We also generated a rat strain, which carried the in-frame mutation in 5' region of *Dmd*. As far as the authors know, rats carrying in-frame mutation in *Dmd* have not been reported, and thus, would be expected to mirror the human BMD pathology better than the previously described mouse model (McCourt et al., 2018). Moreover, 5′ region of the *Dmd* gene (exon 2-20) is one of the mutational hot spots responsible for DMD or BMD which account for approximately 15% of all exon deletions and approximately 64% of all exon duplications within the *Dmd* gene (Tuffery-Giraud et al., 2009). Thus, this model is expected to mirror not only the human BMD pathology but also the pathology of the certain number of patients with DMD converted to BMD by exon-skipping treatment.

In this study, we analyzed the muscular pathology in a newly established rat strain carrying in-frame mutations in the *Dmd* gene. Further, we examined whether this mutation causes the pathology observed in human patients with BMD.

Results

Establishment of a rat strain carrying in frame mutation in the 5' region of *Dmd*

As we previously reported, mutations were induced in rat *Dmd* with CRISPR/Cas in ten F0 dystrophin-mutated male rats (Nakamura et al., 2014). Simultaneously, a F0 *Dmd*-mutated female rat carrying a long-deletion in exon 3-16 was acquired. In this study, we used a rat strain carrying this deletion established by crossing the F0 female rat with the wildtype Wistar Imamichi rats. First, we checked the *Dmd* and mRNA sequence in this rat strain. Sequencing analysis and genomic PCR revealed that they inherited the deletion ranging from exon 3 to 16 (- 324,981 bp) in rat *Dmd* genome sequence (Fig. 1A, 1C). Next, sequencing

analysis and RT-PCR showed that *Dmd* mRNA expression lacked the sequence from exon 3 to 16 (- 1,902 bp), caused by the splicing switch sites (Fig. 1B, 1D). Since the presence of in-frame *Dmd* mRNA was confirmed, this strain was designated as the IF (in-frame) strain. Exon 3-16 of *Dmd* translated into the part of calphonin homology domain 1 (CH1), entire CH2 domain, which are sub-domains of N-terminal actin-binding domain 1, and the first two and part of the third spectrin-like repeats. The predicted molecular structure of tdp427 is shown in Figure 1E.

IF rats show typical dystrophic histopathology in skeletal muscles, but not obvious functional deficiency

In patients with DMD and BMD, the appearance of tissue dystrophic phenotypes, such as continuous muscle degeneration and enhancement of intramuscular fibrosis/ adipogenesis, result in muscle tissue dysfunction.

To study whether IF rats exhibit dystrophic phenotypes in skeletal muscles, pathological evaluations were conducted.

First, we compared two muscle injury markers of IF rats to age-matched WT controls. Serum creatine kinase (CK) is the most frequently used muscle injury marker. Additionally, titin fragment in urine has been described as a new non-invasive biomarker reflecting muscle tissue injury (Matsuo et al., 2019). In our study, both serum CK and urinary titin levels were significantly elevated in IF rats of all ages (Fig. 2A, 2B), indicating that skeletal and/or cardiac muscle were continuously affected.

Next, we analyzed the tissue pathology of skeletal muscles in IF rats. Since fast-twitch myofibers are more affected in dystrophic muscles (Selsby et al., 2012; Webster et al., 1988), we focused on the tibialis anterior (TA) muscle, which is primarily composed of fast-twitch myofibers. Hematoxylin-Eosin staining on TA muscle showed the appearance of lesions containing degenerated fibers and invasion of inflammatory cells irrespective of

animal age (Fig. 2C, Fig. S1A). In addition, the accumulation of intramuscular fibrous tissue was observed in all ages investigated (Fig. 2C, Fig. S2A, B) and intramuscular adipose tissue was observed at the later stage of the disease (11 months) (Fig. 2C, Fig. S2C, D). In addition, embryonic myosin heavy chain (eMHC)-positive regenerating fibers were present only in IF tissues (Fig. 2C, Fig. S1B) and the number of eMHC-positive fibers per section decreased at the age of 11 months of age (Fig. S1C), indicating that the regenerative capacity is kept until six months of age and decreases at 11 months of age. Next, to compare the number of myogenic cells contributing muscle regeneration at six months of age with at 11 months of age, we analyzed the number of Pax7(+) myogenic cells in primary culture derived from extensor digitorum longus muscles (EDL) of 6- and 11-month-old WT and IF rats (Fig. S1D). As a result, there was no significant difference in the number of Pax7(+) cells per well between the genotypes at six months of age, whereas the number was significantly lower in IF than WT at 11 months of age, implying that the potential number of myogenic cells decreases in 11-month-old IF skeletal muscles. These results indicate that IF rats displayed typical dystrophic histopathological characteristics represented by muscle degeneration, followed by muscle regeneration, and fibrosis and adipose tissue infiltration. Moreover, the regenerative capacity decreases at 11 months of age, which may be caused by the decrease of myogenic cells.

Presumably, due to continuous pathological changes, TA muscles of IF rats were significantly heavier than age-matched WT at the late stage of disease (6, 11, and 15 month) (Fig. 2D), despite comparable body weights between genotypes (Fig. S3). To analyze whether muscle fiber hypertrophy occurred in TA muscle, we analyzed the distribution of minimal Feret diameter, which reflects the diameter of each muscle fiber (Briguet et al., 2004). At two months of age, the mean minimal Feret diameter of IF rats was significantly lower than in WT rats (Fig. 2E), indicating the appearance of small regenerating fibers. In contrast, at six months of age, the mean diameter was higher in IF rats (Fig. 2E). This may

reflect the appearance of large regenerated myofibers with age, as observed in skeletal muscles of mdx mice (Sacco et al., 1992). To examine whether the dystrophic effect was also seen in slow-twitch fiber-rich muscle, the weight and the distribution of minimal Feret diameter of the soleus (SOL) muscle was analyzed. Our results showed that unlike TA muscle, the increase in weight was not observed in SOL muscle until 15 months of age (Fig. 2D). Moreover, the mean minimal Feret diameter of IF rats was significantly lower than in WT rats at 2, 6, and 11 months of age (Fig. S4), reflecting the appearance of small regenerating fibers. These results indicate that fast type fibers were readily affected.

Next, to evaluate the muscle strength *in vivo*, we conducted the grip test to evaluate forelimb strength, and the four-limb hanging test to evaluate the whole-body motor skills, at different ages. We did not detect any significant difference in maximum strength in 10 trials of the grip test at all ages (Fig. 2F). Further, no significant difference was detected in results of four-limb hanging tests between genotypes (Fig. 2G). Collectively, skeletal muscle of IF rats showed the dystrophic phenotype represented by muscle degeneration, increased interstitial fibrous/adipose tissue, and muscle hypertrophy, but did not exhibit altered functional deficiency.

IF rats display histopathological changes in cardiac muscles, but not functional deficiency

Patients with BMD frequently display cardiac involvement, and cardiomyopathy represents the number one cause of death of patients with BMD who live until the fifth or sixth decade of life (Finsterer and Stöllberger, 2003).

To explore whether IF rats displayed cardiac failure, we conducted histopathological analyses of cardiac muscles and functional evaluation using echocardiography. The heart weight did not differ between genotypes at all ages investigated (Fig. 3A). However, in the cardiac muscle tissue of IF rats, inflammatory lesions were observed at all ages, indicating

continuous cardiac muscle tissue degeneration (Fig. 3B, Fig. S4A). Further, increased myocardial fibrosis was observed in cardiac muscles of IF animals (Fig. 3C). Also, the fibrotic area percentage increased with age both in right and left ventricle walls in IF animals, whereas that of WT did not significantly change with age (Fig. 3D, Fig. S4B). Subsequently, we evaluated the cardiac function using echocardiography in 7th and 16th months (Table. S1). Our results showed that the heart rates did not differ between genotypes. Functionality of the right and left sides of the heart of IF rats was evaluated by comparing echocardiographic variables with age-matched WT animals. Almost all left-heart variables investigated, such as wall thickness, LV diameters, LV fractional shortening, LV transmitral E, and tissue Doppler imaging (TDI) peak systolic mitral annulus velocity (Sm) in septum, did not differ significantly between the genotypes. These results suggest that the tissue pathological changes do not result in obvious cardiac dysfunction in IF rats. In contrast, we observed significant differences in TDI Sm lateral wall at 16 months of age. This may reflect the promoted fibrotic lesion observed in the outer area of the left ventricular free wall of the IF rats. The left ventricular diastolic index, TDI peak early diastolic mitral annulus velocity (Ea), and Transmittal E / Ea were also evaluated but no significant difference was observed. Further, there was no significant difference in the LV myocardial performance index that reflects both systolic and diastolic capacity, suggesting that the IF left ventricular systolic capacity and diastolic capacity are relatively maintained in IF and WT animals.

No significant differences were observed between genotypes in all right heart variables analyzed. However, RV fractional area change, TAPSE (tricuspid annular plane systolic excursion), and Sm RV free-wall, which are the indexes for RV systolic function, uniformly tended to decrease in 17-month-old IF rats. These results raise the possibility that, in particular, right heart dysfunction occurs in IF rats after 17 months of age, reflecting promoted fibrosis in the right ventricle wall.

Collectively, the cardiac muscles of IF rats exhibited progressive histopathological changes represented by fibrosis. However, no obvious dysfunction was detected in most variables even at the later stage of the disease, although several variable showed a significant difference or declining trend.

Expression of truncated dystrophin is significantly reduced in skeletal muscles of IF rats

In-frame mutations in *DMD* generally result in decreased expression of tdp427 and DGC components compared with healthy controls (Beggs et al., 1991).

We determined the expression of dystrophin and components of DGC (αSG, βDG, nNOS) on skeletal muscles of IF rats using immunohistochemistry and immunoblot analyses. Immunostaining on tibialis anterior (TA) muscles showed that in both, WT and IF rats, the dystrophin and DGC-positive regions were localized beneath the sarcolemma (Fig. 4A). Immunoblot analysis showed that full-length dystrophin in IF skeletal muscles was truncated to a lower molecular weight (~350 kDa) based on genetic mutations (Fig. 4B). In addition, expression of truncated dystrophin was reduced to around 10% of WT despite adequate gene expression (Fig. 4C, D). Immunoblot analysis showed that expression levels of βDG were significantly reduced and those of αSG were slightly reduced in IF skeletal muscles (Fig. S5).

Next, to examine whether the decrease of tdp427 is mediated by enhanced proteasomal degradation, myotubes derived from WT and IF rats were treated with the proteasome inhibitor MG-132 *in vitro*, and the protein level of dp427/tdp427 were measured using immunoblot analysis. As proteasome inhibition completes, dp427/tdp427 levels were recovered (Fig. 4E); moreover, no enhanced protein recovery was observed in IF myotubes compared with WT myotubes (Fig. 4F), suggesting that the expression level of both dp427 and tdp427 is controlled by proteasomal degradation, but a different mechanism was responsible for the reduction of tdp427 in IF skeletal muscles.

These results indicate that in-frame deletion in *Dmd* results in the expression of truncated dystrophin and the reduction of truncated dystrophin and DGC components in skeletal muscle tissues. Moreover, in vitro situation the reduction of tdp427 is not caused by enhanced proteasomal degradation.

Additional dystrophin is specifically expressed in skeletal/cardiac muscle tissues of IF rats

Mutations in *DMD* not only trigger abnormal expression of dp427, but on occasion results in the appearance of unidentified proteins, such as novel dystrophin isoforms (Wein et al., 2014) or additional dystrophin, which is possibly a degradation product of dp427 (Beggs et al., 1992; Hoffman et al., 1988). To explore whether such unidentified proteins appear in IF skeletal muscles, we performed immunoblotting experiments with anti-dystrophin antibody and focused on the detected bands with a molecular weight lower than 427 kDa. As a result of immunoblot analysis with anti C-terminal domain of dystrophin antibody (ab154168), 71 kDa dystrophin isoform (dp71), which is a ubiquitously expressed isoform (Kawaguchi et al., 2018; Tadayoni et al., 2012), was detected in skeletal muscle lysate of both genotypes (Fig. 5A). Additional 75 kDa signals (dpX) were detected in IF rats, but not in WT rats (Fig. 5A). To predict the molecular structure of dpX, comparative immunoblot experiments were performed using different anti-dystrophin antibodies. dpX was detected with another anti C-terminal domain antibody (NCL-dys2) but not with anti-rod domain antibody (NCL-dys1) (Fig. 5B), indicating that dpX possesses the C-terminal structure of dp427 but lacks the proximal rod domain. These results suggested that dpX possesses a partial structure of dp427 and is possibly an unidentified novel dystrophin isoform or a degradation product of tdp427. dp427 is tissue-specifically expressed in skeletal/cardiac muscle and brain (Blake and Kröger, 2000; Nudel et al., 1989). Thus, we next explored whether dpX is present or not in cardiac muscle and brain, namely, tissues expressing dp427

other than skeletal muscle. As a result, we detected dp427/tdp427 expression both in cardiac muscle and brain, whereas dpX was only detected in cardiac muscles of IF rats (Fig. 5C). These results indicate that dpX is expressed only in tdp427-expressing muscle tissues.

Additional dystrophin (dpX) connects to beta-dystroglycan on sarcolemma

C-terminal structure of dp427 is essential for DGC formation mediated by binding with a transmembrane DGC component, β-dystroglycan (βDG) (Rentschler et al., 1999). Thus, we performed DGC pulldown using immunoprecipitation with anti βDG-antibody to examine whether dpX contributes to DGC formation. Prior to this experiment, we confirmed that most dpX was included in the membrane fraction (Fig. 6A, B) using an immunoblot experiment. The pulldown analysis revealed that dp427 in WT and tdp427 in IF co-immunoprecipitated with βDG using the anti-βDG antibody (Fig. 6C), indicating that in-frame mutations affecting N-terminal regions do not necessarily affect dp427-βDG binding. In addition, dpX co-immunoprecipitated with βDG, indicating that dpX binds to βDG directly and is a component of DGC (Fig. 6C).

Collectively, these results imply that dpX is a newly discovered DGC component in skeletal muscles of IF rats.

Discussion

In this study, we established a novel rat model that carries in-frame mutations in *Dmd* (IF rats) and exhibits reduced expression of truncated dystrophin. Our results showed that the abnormal dystrophin expression resulted in the dystrophic changes in muscle tissues, but did not lead to functional deficiency. We also found that the expression of additional dystrophin (dpX), which forms the DGC in sarcolemma, was associated with the appearance of tdp427.

Expression of tdp427 in muscle tissues is one of the factors to determine disease the BMD severity (Anthony et al., 2011; Van Den Bergen et al., 2014). Reports using *in vitro* or transgenic mice models have shown that the point mutations in the 5' region of *DMD* results in the ubiquitin-proteasome system-mediated degradation of mutated dp427 (Singh et al., 2010; Talsness et al., 2015). However, our study demonstrated that although the expression level of tdp427 was significantly reduced in skeletal muscles, the proteasomal degradation was not enhanced when compared to dp427 *in vitro*. These results indicate that the difference in the instability of tdp427 and dp427 is not due to the change in tertiary structure. Therefore, a different mechanism may underlie the decrease in the tdp427 levels. However, it should be noted that the proteasomal inhibition in this study is under the limited situation *in vitro*. Further research is needed to clarify the mechanism underlying the decrease of tdp427 *in vivo* environment of IF muscle tissues. A previous study has reported that TNFα-induced microRNAs control dystrophin expression in Becker muscular dystrophy (Fiorillo et al., 2015). As the continuous inflammation was observed in IF skeletal muscles, it is possible that the inflammation-related microRNAs contribute to the decrease of tdp427. Furthermore, several reports have indicated that the forced expression of dystrophin isoforms (dps), which have the same C-terminal structure as dp427, can compete with it for sarcolemma binding, thereby decreasing the levels of dp427 in WT skeletal muscles (Leibovitz et al., 2002; Warner, 2002). In the present study, we demonstrated that dpX contained the C-terminal structure of dp427, and both, tdp427 and dpX, localized in sarcolemma and formed DGC. Therefore, not only microRNA but also dpX may contribute to the decrease of tdp427 in skeletal muscles of IF rats by competing with tdp427 on the sarcolemma in the same manner as dps.

Our results did not elucidate the mechanism underlying the disease-specific expression of dpX in IF muscle tissues. However, according to the previous reports, the expression of dpX may be regulated at pre- and/or at post-transcriptional levels of *Dmd*

mRNA. The retention of intronic sequence in mature *DMD* mRNA has been reported in the patients with DMD (Nishida et al., 2015). In addition, mutations in *DMD* occasionally result in the appearance of novel dystrophin isoforms caused by the alternative translation initiation (Wein et al., 2014). As similar as these reports, *Dmd*-mutation in IF rats possibly causes the intron retention in *Dmd* mRNA or the alternative translation initiation. Also, intron retention may trigger the unpredicted splicing on *Dmd* mRNA, which leads to the expression of dpX in the muscle tissues of IF rats. Furthermore, it has been reported that skeletal muscle biopsies from human patients with BMD, whose mutations are located in the distal rod domain (exon 45-53), show additional dystrophin expression (Beggs et al., 1992; Hoffman et al., 1988). The authors concluded that the additional dystrophin is a proteolytic product of tdp427. In the present study, we demonstrated that dpX contained the C-terminal structure of dp427 and dpX expression was restricted to tdp427-expressing tissues, except for the brain. These results indicate that dpX could be a breakdown product of tdp427, like additional human dystrophin. A previous *in vitro* study demonstrated that calcium-dependent proteases, calpain Ⅰ and II cleave dp427 into products of different sizes (Cottin et al., 1992). It is possible that in the muscle tissues of IF rats such proteases are more activated than in that of healthy control as reported in the skeletal muscles of mdx mice (Gailly et al., 2007). Additionally, the function of dpX in muscle tissues also remains unknown. In the present study, we demonstrated that both, tdp427 and dpX, localized in sarcolemma and formed DGC. As dp71-mediated DGC restoration did not ameliorate the pathology of mdx mice (Cox et al., 1994), it is conceivable that dpX, which may have a similar molecular weight and structure as dp71, also plays little ameliorating role in IF muscle tissues. Collectively, our data implies that the endogenous additional dystrophin, such as dpX, whose expression is triggered by in-frame mutations in *Dmd*, may restore DGC on the sarcolemma. Further research is required to reveal the mechanism underlying the appearance of dpX and the function of dpX.

In our previous study, the dystrophin deficient (DMD) rats exhibited muscle tissue pathology similar to of muscular dystrophy, represented by the continuous muscle degeneration and deposition of intramuscular fibrous tissues and fat; further, the animals showed noticeable decreased in the muscle strength at 13 weeks of age (Nakamura et al., 2014). In contrast, the IF rats did not show any detectable impaired function in the skeletal and cardiac muscles despite the presence of tissue pathological changes similar to DMD rats. Further, in muscle tissues, we confirmed the expression of tdp427 that lacked the region corresponding to the mutated DMD protein. These findings imply that tdp427-lacking domains, encoded by exon 3-16, do not function as sarcolemma-supporting proteins enough to prevent histological lesions, but functional enough to ensure normal force generation by muscle tissue. Recently, the role of dystrophin in neuromuscular junctions (NMJs) has become clearer. NMJ is a specialized synapse formed between the terminal end of a motor neuron and a muscle fiber to transmit the nerve impulses to muscles. The impaired function of muscle tissues, represented by the decrease in muscle strength and easy fatigability, is considered to be triggered by NMJ abnormalities. It is reported that the dystrophin is enriched post-synaptically at NMJs and aids neuromuscular transmission (Bewick et al., 1992). The absence of dystrophin at NMJs in mdx mice causes neuromuscular transmission defects that aggravate muscle weakness (van der Pijl et al., 2016). Although it remains unclear which dystrophin domain is important for NMJ functionality, the tdp427 in IF rats, even with a missing part of the protein, might be sufficient for normal NMJ function. This might explain the lack of functional deficiency in IF rats.

In conclusion, the present study demonstrated the usefulness of the novel rat BMD model in reflecting the tissue pathology associated with the human BMD. Furthermore, our results provide the expression profile of novel dystrophin-related product (dpX) in BMD with mutations within the 5' region in the *DMD* gene. Although the IF rats described in the present study do not entirely cover the overall pathology seen in human BMD showing variable

pathological states among individuals, the outcome of the present study further the understanding of BMD pathology, and indicate the possibility of dystrophin recovery treatments for patients with DMD.

Materials and Methods

Animals

A rat strain carrying in-frame mutations in the *Dmd* gene (IF strain) was maintained in our laboratory under controlled environmental conditions: 23°C with a photoperiod of 12-h light and 12-h dark (lights on at 0800 h). This strain was derived from a female rat which is a littermate of *Dmd*-mutated F0 rats previously reported (Nakamura et al., 2014) . The female IF rat was mated with the male Wistar-Imamichi strain purchased from the Institute for Animal Production (Ibaraki, Japan) to maintain the strain. IF and age-matched WT males were used in this study. Animals were fed commercial chow *ad libitum* (Lab MR-Breeder Standard, Nihon Nosan Kogyo, Yokohama, Japan). All animal experiments in this study were performed in accordance with the Guide for the Care and Use of Laboratory Animals of the University of Tokyo and were approved by the Institutional Animal Care and Use Committee of the University of Tokyo (certificate No. P18-125).

RT- PCR

After TA muscles were homogenized using a Shake Master (ver. 1.0, Bio Medical Science Inc., Tokyo, Japan), RNA was isolated using TRIzol (Invitrogen, Carlsbad, CA, USA) and reverse-transcribed to cDNA using SuperScriptII reverse transcriptase (Invitrogen). Quantitative RT-PCR (qPCR) was performed using a Light Cycler 2.0 (Roche Diagnostics, Roche, Basel, Switzerland) with Thunderbird SYBR qPCR Mix (TOYOBO, Osaka, Japan). The sequences of the primer sets used in RT-PCR and qPCR are listed in Supplementary table 2.

Sequencing analysis

Genomic DNA and cDNA were obtained from TA muscles. PCR was performed to confirm deletion of *Dmd* gene and *Dmd* mRNA. PCR products were purified by agarose gel electrophoresis and subsequently sequenced as previously reported (Fujii et al., 2013).

Histological analyses

Histological analyses were performed using a previously published method (Nakamura et al., 2014). Briefly, frozen sections (7-μm thick) of Tibialis Anterior (TA) muscles were prepared transversely, and paraffin-embedded sections of the heart were subjected to histological analyses. The sections were used for hematoxylin and eosin (H&E) and Masson's trichrome staining, dehydrated, and mounted.

For immunostaining, cryosections were fixed with 4% paraformaldehyde. After blocking with 5% normal donkey serum in phosphate-buffered saline (PBS) containing 0.1% Triton X-100 (Sigma-Aldrich, St. Louis, MO, USA), cryosections were incubated overnight with primary antibodies (described below) at 4°C, followed by washing and incubation with AlexaFluor-conjugated secondary antibodies (1:500, Jackson ImmunoResearch, West Grove, PA, USA) for 1-h. Nuclei were counterstained with Hoechst 33258. For quantitative analyses of the fibrotic area, 5 to 20 fields were randomly selected in the sections with Masson Trichrome staining using a 10× objective for skeletal muscles and a 4× objective for cardiac muscles. The area occupied by fibrotic tissues stained blue and the total area of sections were calculated using ImageJ software. For quantitative analyses of myofiber diameters, 10 fields in TA and 5 fields in SOL were randomly selected in the sections stained with anti-laminin antibody using a 10x objective. The minimal Feret's diameter was calculated using ImageJ software. For quantitative analyses of eMHC-positive fibers, the number of positive fibers per section was counted under the microscope. Photos were taken under a fluorescence

microscope (BX51, Olympus, Tokyo, Japan) equipped with a digital camera (DP73, Olympus).

Primary antibodies and their species of origin were as follows: anti-dystrophin (rabbit monoclonal, ab154168, 1:400, Abcam, Cambridge, UK), anti-laminin (rabbit polyclonal, L9393, 1:100, Sigma-Aldrich), anti-eMHC (mouse monoclonal, F1.652, 1:100, Developmental Studies Hybridoma Bank, Iowa City, IA, USA), anti-α-sarcoglycan (mouse monoclonal, AD1/20A6, 1:100, Novocastra, Newcastle upon Tyne, UK), anti-β-dystroglycan (mouse monoclonal, 43DAG1/8D5, 1:100, Novocastra), and anti-nNOS (rabbit polyclonal, 1:100, Invitrogen).

Immunoblotting

TA muscles were lysed in RIPA buffer [50 mM Tris-HCl pH 7.4, 1% NP-40, 0.5% Na-deoxycholate, 0.1% sodium dodecyl sulfate (SDS), 150 mM NaCl, 2 mM EDTA, and 50 mM NaF]. For perilipin detection, sample buffer [0.5 M Tris-HCl, 10% glycerol, 1% SDS, and 10% 2-mercaptoethanol] was used during homogenization. Protein concentration was determined using the bicinchoninic acid assay reagent (Fuji film-WAKO, Osaka, Japan). Equal amounts of protein were resolved on a 10% polyacrylamide gel and subsequently transferred onto a polyvinylidene difluoride (PVDF) membrane (Millipore). The membranes were blocked with 5% skim milk in Tris-buffered saline containing 0.1% Tween and incubated with primary antibodies (described below) overnight at 4˚C, followed by incubation with horseradish peroxidase (HRP)-conjugated secondary antibodies (1:5,000) for 1-h at room temperature. Protein bands were detected using enhanced ECL prime (GE Healthcare UK Ltd., Buckinghamshire, England) and a ChemiDoc™ (Bio-Rad, Hercules, CA, USA). The band intensity was determined using Image Lab™ software (Bio-Rad). Primary antibodies used in the experiments were as follows: anti-Dystrophin (rabbit monoclonal, ab154168, 1:400, Abcam), NCL-dys1 (mouse monoclonal, 1:100, Novocastra),

NCL-dys2 (mouse monoclonal, 1:100, Novocastra), anti-α-sarcoglycan (mouse monoclonal, AD1/20A6, 1:100, Novocastra), anti-β-dystroglycan (mouse monoclonal, 7D11, 1:400, Santa Cruz biotechnology), anti-perilipin (rabbit monoclonal, D1D8, 1:1000, Cell Signaling, Danvers, MA, USA), anti-α-tubulin (rabbit polyclonal, ab4074, 1:660, Abcam), and anti-β-actin (rabbit monoclonal, 13E5, 1:500, Cell Signaling).

Creatine kinase activity

Whole blood was collected from abdominal aorta under anesthesia with isoflurane and spun at 1,000 x *g* for 30 min at 4˚C. Creatine kinase activity in separated sera was assayed using the Fuji Drychem system (Fuji Film Medical Co. Ltd.; Tokyo, Japan).

Urinary titin

Urine samples were obtained from 3, 4-, and 11-month-old IF rats and age-matched WT rats. Urinary titin was measured using an ELISA system using the Titin-N Fragment Assay Kit-IBL (Immuno-Biological Laboratories Co. Ltd., Fujioka, Japan) (Matsuo et al., 2019), as previously described (Awano et al., 2018). Urinary creatinine (Cr) concentrations were measured using an assay kit (LabAssay Creatinine, Wako Pure Chemical Industries, Ltd., Osaka, Japan). This kit detects both titin-N fragments of skeletal and cardiac muscles (Yoshihisa et al., 2018).

Skeletal muscle function

Grip test

Grip test was performed to evaluate strength of forelimb muscles. The method complies with the modified version of "Use of grip strength meter to assess the limb strength of mdx mice" (TREAT-NMD SOP ID: DMD_M.2.2.001) (Bladen et al., 2015). Briefly, rats were placed with their forelimbs on a T-shaped bar and were gently pulled backward until they

released their grip. A grip meter (GPM-101B, MELQUEST, Toyama, Japan) measured the peak force generated. Ten tests were performed in sequence with a short latency between each test, and the maximum strength in ten trials was taken as an index of grip strength. Results are expressed as a percentage of the body weight (g/g).

Four limb hanging test

Four limb hanging test was performed to evaluate the strength of four limb muscles. The method complies with the modified version of "The use of four limb hanging tests to monitor muscle strength and condition over time" (TREAT-NMD SOP ID: DMD_M.2.1.005) (George Carlson and van Putten, 2011). Briefly, Each rat was allowed to use its four limbs to grasp an aluminum mesh (35 cm x 45 cm, 1.5 x 1.5 cm square grid), which was placed vertically 1 m above a cushion. The time to fall was recorded and the value was multiplied by the body weight as an indication of muscle strength. A fixed limit was applied in hanging-time (a maximum of 60 seconds). The records of rats who climbed over the top of the aluminum mesh and stayed still there were omitted from data.

Echocardiography

Echocardiographic images were acquired using a Vivid E95 digital ultrasound system (GE Vingmed Ultrasound, Horten, Norway) with a 12 MHz 12S-D probe (GE Vingmed Ultrasound) on 7 and 16-month-old WT and IF rats. Echocardiographic images were analyzed with EchoPac (GE). Rats were anaesthetized with isoflurane at a concentration of 5%. Rats were then placed on a heated platform, and anesthesia was maintained by 3-4% isoflurane. Under anesthesia, echocardiographic images were acquired. Images of the parasternal short-axis view at the papillary muscle level and the apical 4-chamber view were recorded to obtain a higher frame rate (about 200 frames per second) with higher imaging qualities. For assessing LV diastolic function, early diastolic velocity peak (E) and late

diastolic peak (A) were measured along the short axis view using Tissue Doppler Mode. A wave was not detectable in this study. For assessing LV systolic function, fractional shortening, and ejection fractions were calculated by measuring intraventricular septum thickness in diastole, LV posterior wall thickness, LV end-diastolic, and end-systolic diameters. These values were measured along the parasternal short axis view in Motion mode (Mmode). LV Myocardial performance index (MPI), a universal value of ventricular systolic and diastolic function, was determined using Tissue Doppler Mode. For calculating MPI, aortic ejection time and the non-flow time of the left ventricle were measured. Fractional area change (FAC) and tricuspid annular plane systolic excursion (TAPSE) were evaluated as variables for RV function.

***In vitro* myogenic cell isolation: analysis of myogenic cell numbers or proteasome inhibition**

Skeletal muscle myogenic progenitor cells were obtained from the muscles of WT and IF rats as described previously (Yamanouchi et al., 2007). Briefly, muscles were hand-minced using scissors, and digested for 1-h at 37 °C with 1.25 mg/mL protease (from *Streptomyces griseus*, type XIV; Sigma). Cells were separated from muscle-fiber fragments and tissue debris through differential centrifugation and plated on poly-L-lysine- and fibronectin-coated plates in 10% FBS/DMEM. As for the analysis of myogenic cell numbers, extensor digitorum longus muscles (EDL) of 6- and 11-month-old WT and IF rats were used. Cells separated from one side of EDL were dispensed into 2 wells of 48-well-plate. After 2-day culture in the medium (10% FBS/DMEM), cells were fixed with 4% paraformaldehyde, blocked with 5% normal goat serum in PBS containing 0.1% Triton X-100 (Sigma), and incubated overnight with anti-Pax7 antibodies (mouse monoclonal, P3U1, 1:100, Developmental Studies Hybridoma Bank) at 4 °C and then for 1 h with AlexaFluor-conjugated secondary antibodies (1:500, Invitrogen). As for the proteasome inhibition, back and hind-limb muscles of neonatal

rats (day 0-1) were used. After 7-day culture in the medium (10% FBS/DMEM), the proteasome inhibitor MG-132 (Enzo Life Sciences, Farmingdale, NY, USA) or DMSO as control were added at a concentration of 5 μg/mL in the media on WT and IF myotubes differentiated from obtained myogenic progenitor cells. Total protein lysate was extracted with sample buffer after 24-h culture with MG-132/DMSO.

Separation of membrane fraction

One half of frozen TA muscle was homogenized in ice cold homogenization buffer [10% Sucrose, 0.5 mM EDTA, 1 mM PMSF, pH7.2, and 0.2% protein inhibitor cocktail (Promega)] using a tissue homogenizer (Kinematica Polytron, Lucerne, Switzerland). Samples were then centrifuged at 12,000 x *g* for 10 min at 4˚C and the supernatant was discarded. To extract the membrane fraction, pellets were resuspended in extraction buffer [50 mM Tris-HCl (pH 7.4), 150 mM NaCl, 0.05% NP-40, 1% digitonin, and 0.2% protein inhibitor cocktail] for 1-h on ice and then centrifuged at 20,000 x *g* for 30 min at 4˚C to remove the insoluble residue.

Co-immunoprecipitation

The separated membrane fraction was pre-cleared of mouse antibody by incubation with Protein G agarose beads (sc-2002, Santa Cruz biotechnology) for 30 min at 4°C, followed by centrifugation at 5,000 x *g* to remove resin. To conjugate protein G with antibodies, protein G agarose beads (50 μL, sc-2002, Santa Cruz biotechnology) were incubated with anti-βDG antibody (7D11, Santa Cruz biotechnology, 5 μg for βDG IP) and isotype matched mouse IgG (G3A1, Cell Signaling, 5 μg for control IP) in PBS [150 mM NaCl, 8 mM NaH2PO4, and 42 mM Na2HPO4, pH 7.5] overnight at 4 ˚C. Thereafter, the beads were washed three times with PBS. Next, 200 μg of pre-cleared protein lysate was added to 7D11 or G3A1 conjugated protein G agarose beads and the mixture was incubated overnight at 4 ˚C in end-

over-end mixing. After the incubation, supernatant was collected as unbound fraction. Beads were washed three times with PBS. Sample buffer was used for elution.

Statistical analyses

A Student's *t*-test and one-way ANOVA followed by Tukey Kramer's test were used to examine statistical differences between two groups and more than two groups, respectively. For the distribution of myofibers, median values were compared using the Wilcoxon rank sum test. *P*-values less than 0.05 were considered statistically significant. Graphed data represent means + SDs.

Acknowledgements

We would like to thank Editage (www.editage.com) for English language editing.

Competing interests

No competing interest declared.

Funding

This work was supported by the Grant-in-Aid for JSPS Research Fellows [17J08505 to N.T.]; Grant-in-Aid for Challenging Exploratory Research [15K14883 to K.Y.]; Grant-in-Aid for Scientific Research (B) [16H05041 to K.Y.]; and Grant-in-Aid for Scientific Research (C) [17K07092 to K.K.], from Japan Society for the Promotion of Science.

References

Anthony, K., Cirak, S., Torelli, S., Tasca, G., Feng, L., Arechavala-Gomeza, V., Armaroli, A., Guglieri, M., Straathof, C. S., Verschuuren, J. J., et al. (2011). Dystrophin quantification and clinical correlations in Becker muscular dystrophy: Implications for clinical trials. In *Brain*, pp. 3544–3556. Oxford University Press.

Awano, H., Matsumoto, M., Nagai, M., Shirakawa, T., Maruyama, N., Iijima, K., Nabeshima, Y. ichi and Matsuo, M. (2018). Diagnostic and clinical significance of the titin fragment in urine of Duchenne muscular dystrophy patients. *Clin. Chim. Acta* **476**, 111–116.

Beggs, A. H., Hoffman, E. P., Snyder, J. R., Arahata, K., Specht, L., Shapiro, F., Angelini, C., Sugita, H. and Kunkel, L. M. (1991). Exploring the molecular basis for variability among patients with Becker muscular dystrophy: Dystrophin gene and protein studies. *Am. J. Hum. Genet.* **49**, 54–67.

Beggs, A. H., Hoffman, E. P. and Kunkel, L. M. (1992). Additional dystrophin fragment in Becker muscular dystrophy may result from proteolytic cleavage at deletion junctions. *Am. J. Med. Genet.* **44**, 378–381.

Bewick, G. S., Nicholson, L. V., Youngr, C., Odonnell, E. and Slater, C. R. (1992). Different distributions of dystrophin and related proteins at nerve-muscle junctions. *Neuroreport* **3**, 857–860.

Bladen, C. L., Salgado, D., Monges, S., Foncuberta, M. E., Kekou, K., Kosma, K., Dawkins, H., Lamont, L., Roy, A. J., Chamova, T., et al. (2015). The TREAT-NMD DMD global database: Analysis of more than 7,000 duchenne muscular dystrophy mutations. *Hum. Mutat.* **36**, 395–402.

Blake, D. J. and Krǿger, S. (2000). The neurobiology of Duchenne muscular dystrophy: Learning lessons from muscle? *Trends Neurosci.* **23**, 92–99.

Briguet, A., Courdier-Fruh, I., Foster, M., Meier, T. and Magyar, J. P. (2004). Histological parameters for the quantitative assessment of muscular dystrophy in the mdx-mouse. *Neuromuscul. Disord.* **14**, 675–682.

Campbell, K. P. and Kahl, S. D. (1989). Association of dystrophin and an integral membrane glycoprotein. *Nature* **338**, 259–262.

Cottin, P., Poussard, S., Mornet, D., Brustis, J. J. J., Mohammadpour, M., Leger, J., Ducastaing, A., Momet, D., Brustis, J. J. J., Mohammadpour, M., et al. (1992). In vitro digestion of dystrophin by calcium-dependent proteases, calpains I and II. *Biochimie* **74**, 565–570.

Cox, G. A., Sunada, Y., Campbell, K. P. and Chamberlain, J. S. (1994). Dp71 can restore the dystrophin-associated glycoprotein complex in muscle but fails to prevent dystrophy. *Nat. Genet.* **8**, 333–339.

Finsterer, J. and Stöllberger, C. (2003). The Heart in Human Dystrophinopathies. *Cardiology* **99**, 1–19.

Fiorillo, A. A., Heier, C. R., Novak, J. S., Tully, C. B., Brown, K. J., Uaesoontrachoon, K., Vila, M. C., Ngheim, P. P., Bello, L., Kornegay, J. N., et al. (2015). TNF-α-Induced microRNAs Control Dystrophin Expression in Becker Muscular Dystrophy. *Cell Rep.* **12**, 1678–1690.

Fujii, W., Kano, K., Sugiura, K. and Naito, K. (2013). Repeatable Construction Method for Engineered Zinc Finger Nuclease Based on Overlap Extension PCR and TA-Cloning. *PLoS One* **8**, e59801.

Gailly, P., De Backer, F., Van Schoor, M. and Gillis, J. M. (2007). In situ measurements of calpain activity in isolated muscle fibres from normal and dystrophin-lacking mdx mice. *J. Physiol.* **582**, 1261–1275.

George Carlson, A. and van Putten, M. (2011). *The use of four limb hanging tests to monitor muscle strength and condition over time SOP (ID) Number*.

Henderson, D. M., Belanto, J. J., Li, B., Heun-Johnson, H. and Ervasti, J. M. (2011). Internal deletion compromises the stability of dystrophin. *Hum. Mol. Genet.* **20**, 2955–2963.

Heo, Y.-A. (2020). Golodirsen: First Approval. *Drugs*.

Hoffman, E. P., Brown, R. H. and Kunkel, L. M. (1987). Dystrophin: The protein product of the duchenne muscular dystrophy locus. *Cell* **51**, 919–928.

Hoffman, E. P., Fischbeck, K. H., Brown, R. H., Johnson, M., Medori, R., Loire, J. D., Harris, J. B., Waterston, R., Brooke, M., Specht, L., et al. (1988). Characterization of Dystrophin in Muscle-Biopsy Specimens from Patients with Duchenne's or Becker's Muscular Dystrophy. *N. Engl. J. Med.* **318**, 1363–1368.

Kawaguchi, T., Niba, E. T. E., Rani, A. Q. M., Onishi, Y., Koizumi, M., Awano, H., Matsumoto, M., Nagai, M., Yoshida, S., Sakakibara, S., et al. (2018). Detection of dystrophin Dp71 in human skeletal muscle using an automated capillary western assay system. *Int. J. Mol. Sci.* **19**,.

Koenig, M., Monaco, A. P. P. and Kunkel, L. M. M. (1988). The complete sequence of dystrophin predicts a rod-shaped cytoskeletal protein. *Cell* **53**, 219–228.

Koenig, M., Beggs, A. H., Moyer, M., Scherpf, S., Heindrich, K., Bettecken, T., Meng, G., Müller, C. R., Lindlöf, M., Kaariainen, H., et al. (1989). The molecular basis for duchenne versus becker muscular dystrophy: Correlation of severity with type of deletion. **45**, 498–506.

Lapidos, K. A., Kakkar, R. and McNally, E. M. (2004). The dystrophin glycoprotein complex: signaling strength and integrity for the sarcolemma. *Circ. Res.* **94**, 1023–31.

Matsuo, M., Awano, H., Maruyama, N. and Nishio, H. (2019). Titin fragment in urine: A noninvasive biomarker of muscle degradation. In *Advances in Clinical Chemistry*, pp. 1–23. Academic Press Inc.

McCourt, J. L., Rhett, K. K., Jaeger, M. A., Belanto, J. J., Talsness, D. M. and Ervasti, J. M. (2015). In vitro stability of therapeutically relevant, internally truncated dystrophins. *Skelet. Muscle* **5**,.

McCourt, J. L., Talsness, D. M., Lindsay, A., Arpke, R. W., Chatterton, P. D., Nelson, D. M., Chamberlain, C. M., Olthoff, J. T., Belanto, J. J., McCourt, P. M., et al. (2018). Mouse models of two missense mutations in actin-binding domain 1 of dystrophin associated with Duchenne or Becker muscular dystrophy. *Hum. Mol. Genet.* **27**, 451–462.

Nakamura, K., Nakano, S.-I., Miyoshi, T., Yamanouchi, K. and Nishihara, M. (2013). Loss of sparc in mouse skeletal muscle causes myofiber atrophy. *Muscle Nerve* **48**, 791–799.

Nakamura, K., Fujii, W., Tsuboi, M., Tanihata, J., Teramoto, N., Takeuchi, S., Naito, K., Yamanouchi, K. and Nishihara, M. (2015). Generation of muscular dystrophy model rats with a CRISPR/Cas system. *Sci. Rep.*

Nishida, A., Minegishi, M., Takeuchi, A., Niba, T., Awano, H., Lee, T., Iijima, K., Takeshima, Y. and Matsuo, M. (2015). Tissue- and case-specific retention of intron 40 in mature dystrophin mRNA. *Neuromuscul. Disord.* **25**, S253.

Nudel, U., Zuk, D., Einat, P., Zeelon, E., Levy, Z., Neuman, S. and Yaffe, D. (1989). Duchenne muscular dystrophy gene product is not identical in muscle and brain. *Nature* **337**, 76–78.

Rau, F., Lainé, J., Ramanoudjame, L., Ferry, A., Arandel, L., Delalande, O., Jollet, A., Dingli, F., Lee, K.-Y., Peccate, C., et al. (2015). Abnormal splicing switch of DMD's

penultimate exon compromises muscle fibre maintenance in myotonic dystrophy. *Nat. Commun.* **6**, 7205.

Rentschler, S., Linn, H., Deininger, K., Bedford, M. T., Espanel, X. and Sudol, M. (1999). The WW domain of dystrophin requires EF-hands region to interact with β-dystroglycan. *Biol. Chem.* **380**, 431–442.

Rybakova, I. N., Amann, K. J. and Ervasti, J. M. (1996). A new model for the interaction of dystrophin with F-actin. *J. Cell Biol.* **135**, 661–672.

Sacco, P., Jones, D. A., Dick, J. R. T. and Vrbova, G. (1992). Contractile properties and susceptibility to exercise-induced damage of normal and mdx mouse tibialis anterior muscle. *Clin. Sci.* **82**, 227–236.

Selsby, J. T., Morine, K. J., Pendrak, K., Barton, E. R. and Sweeney, H. L. (2012). Rescue of dystrophic skeletal muscle by PGC-1α involves a fast to slow fiber type shift in the mdx mouse. *PLoS One* **7**,.

Singh, S. M., Kongari, N., Cabello-Villegas, J. and Mallela, K. M. G. G. (2010). Missense mutations in dystrophin that trigger muscular dystrophy decrease protein stability and lead to cross-β aggregates. *Proc. Natl. Acad. Sci. U. S. A.* **107**,.

Tadayoni, R., Rendon, A., Soria-Jasso, L. E. and Cisneros, B. (2012). Dystrophin Dp71: The smallest but multifunctional product of the duchenne muscular dystrophy gene. *Mol. Neurobiol.* **45**, 43–60.

Talsness, D. M., Belanto, J. J. and Ervasti, J. M. (2015). Disease-proportional proteasomal degradation of missense dystrophins. *Proc. Natl. Acad. Sci. U. S. A.* **112**, 12414–12419.

Tuffery-Giraud, S., Béroud, C., Leturcq, F., Yaou, R. Ben, Hamroun, D., Michel-Calemard, L., Moizard, M. P., Bernard, R., Cossée, M., Boisseau, P., et al. (2009). Genotype-phenotype analysis in 2,405 patients with a dystrophinopathy using the UMD-DMD database: A model of nationwide knowledgebase. *Hum. Mutat.* **30**, 934–945.

Van Den Bergen, J. C., Wokke, B. H., Janson, A. A., Van Duinen, S. G., Hulsker, M. A., Ginjaar, H. B., Van Deutekom, J. C., Aartsma-Rus, A., Kan, H. E. and Verschuuren, J. J. G. M. (2014). Dystrophin levels and clinical severity in Becker muscular dystrophy patients. *J. Neurol. Neurosurg. Psychiatry* **85**, 747–753.

van der Pijl, E. M., van Putten, M., Niks, E. H., Verschuuren, J. J. G. M. G. M., Aartsma-Rus, A. and Plomp, J. J. (2016). Characterization of neuromuscular synapse function abnormalities in multiple Duchenne muscular dystrophy mouse models. *Eur. J. Neurosci.* **43**, 1623–1635.

Webster, C., Silberstein, L., Hays, A. P. and Blau, H. M. (1988). Fast muscle fibers are preferentially affected in Duchenne muscular dystrophy. *Cell* **52**, 503–513.

Wein, N., Vulin, A., Falzarano, M. S., Szigyarto, C. A. K., Maiti, B., Findlay, A., Heller, K. N., Uhlén, M., Bakthavachalu, B., Messina, S., et al. (2014). Translation from a DMD exon 5 IRES results in a functional dystrophin isoform that attenuates dystrophinopathy in humans and mice. *Nat. Med.* **20**, 992–1000.

Yamanouchi, K., Yada, E., Ishiguro, N. and Nishihara, M. (2007). 18α-Glycyrrhetinic Acid Induces Phenotypic Changes of Skeletal Muscle Cells to Enter Adipogenesis. *Cell. Physiol. Biochem.* **20**, 781–790.

Yoshihisa, A., Kiko, T., Sato, T., Oikawa, M., Kobayashi, A. and Takeishi, Y. (2018). Urinary N-terminal fragment of titin is a marker to diagnose muscular dystrophy in patients with cardiomyopathy. *Clin. Chim. Acta* **484**, 226–230.

Figures

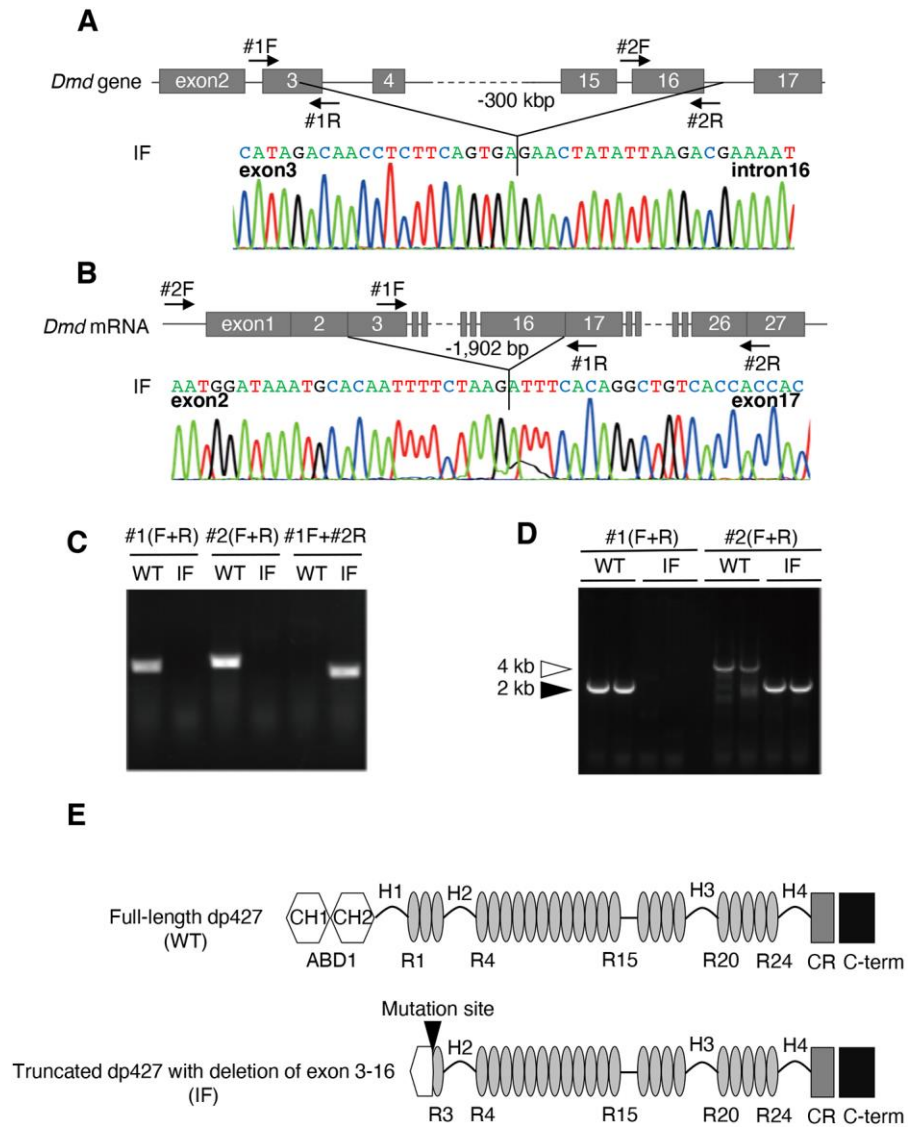

Fig. 1. Overview of *Dmd* gene mutations in IF rats

(A) Sequence of *Dmd* gene of IF rats. Arrows indicate the location of primers used in PCR.

(B) Sequence of mutated *Dmd* mRNA in IF rats. Arrows indicate the location of primers used.

(C) PCR results for *Dmd* gene on genome of WT and IF.

(D) RT-PCR results for *Dmd* gene on cDNA of WT and IF.

(E) The molecular structure of full-length dp427 (upper) and truncated dp427 (below). CH; calponin homology domain, ABD1: actin-binding domain 1, H: Hinge, R: spectrin-like repeat, CR: Cysteine-rich domain, C-ter: C-terminal domain. The black arrowhead indicates the mutation site.

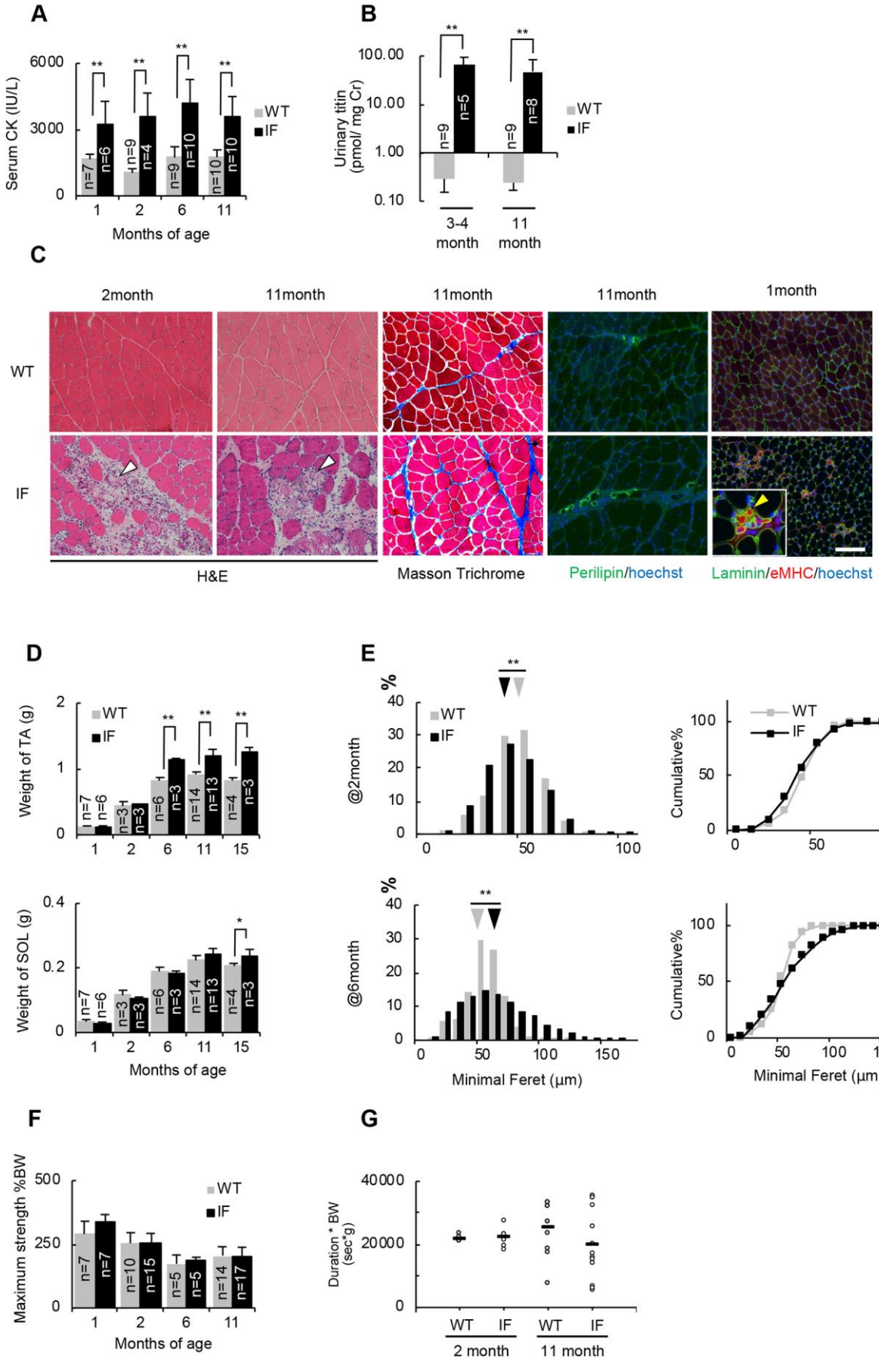

Fig. 2. Phenotypic analysis of skeletal muscles of IF rats

(A, B) Serum creatine kinase (A) and urinary titin (B) activity in WT and IF rats at different ages. Values of urine titin is standardized by the value of urinary creatinine. Data are presented as means+SD. $^{**}P < 0.01$, analysis using *t*-test.

(C) Representative images of H&E staining, Masson trichrome staining, immunostaining of perilipin, and eMHC on TA muscle sections of WT and IF rats at different ages. Scale bar = 50 μm. White arrow heads indicate lesions with degenerated fibers and inflammatory cells. Yellow arrowhead indicates an eMHC-positive regenerated fiber.

(D) Weight of TA and SOL of 1, 2, 6, 11, and 15-month-old WT and IF rats. Data are presented as means+SD. $^{*}P < 0.05$, $^{**}P < 0.01$, analysis using *t*-test.

(E) Relative distributions and cumulative plots of myofiber size in TA in 2 and 6-month-old WT and IF rats. Each arrowhead indicates a median value of each group. The data in each group contains the total number of detected myofibers from 3 subjects per group. $^{**}P < 0.01$, analysis using Wilcoxon rank sum test.

(F) Maximum strength in ten trials of grip-test, standardized by body weight (%) at various ages. Data are presented as means+SD.

(G) Results of four-limb hanging test in 2- and 11-month-old WT and IF rats. n = 5-13, in each group. Bars represent the mean value of each group.

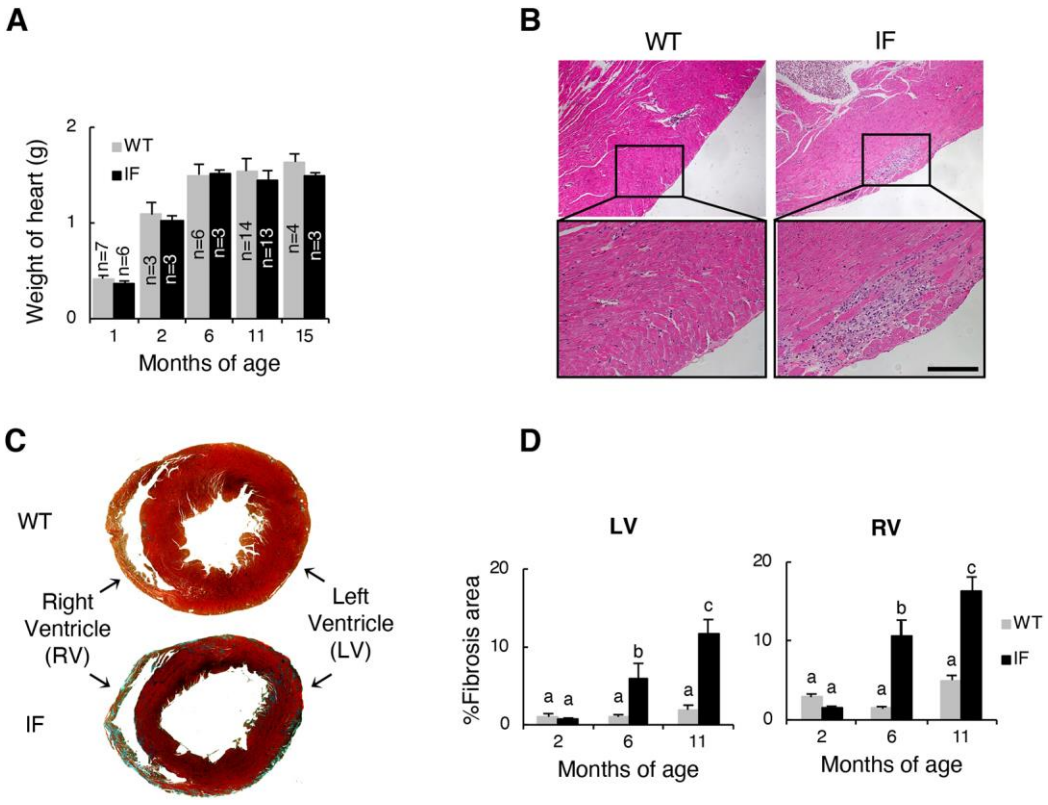

Fig. 3. Histopathology of cardiac muscles of IF rats

(A) Weight of heart of 1, 2, 6, 11, and 15-month-old WT and IF rats. Data are presented as means+SD.

(B) Representative images of HE staining of heart sections of 6-month-old WT and IF rats. Scale bar = 50 μm.

(C) Representative images of Masson Trichrome staining of heart of 11-month-old WT and IF rats.

(D) Quantitative analysis of fibrosis area in left and right ventricle wall of 2, 6, and 11-month-old WT and IF rats (n = 3 in each group). Different letters indicate significant differences between groups ($P < 0.05$, analysis using Tukey's test).

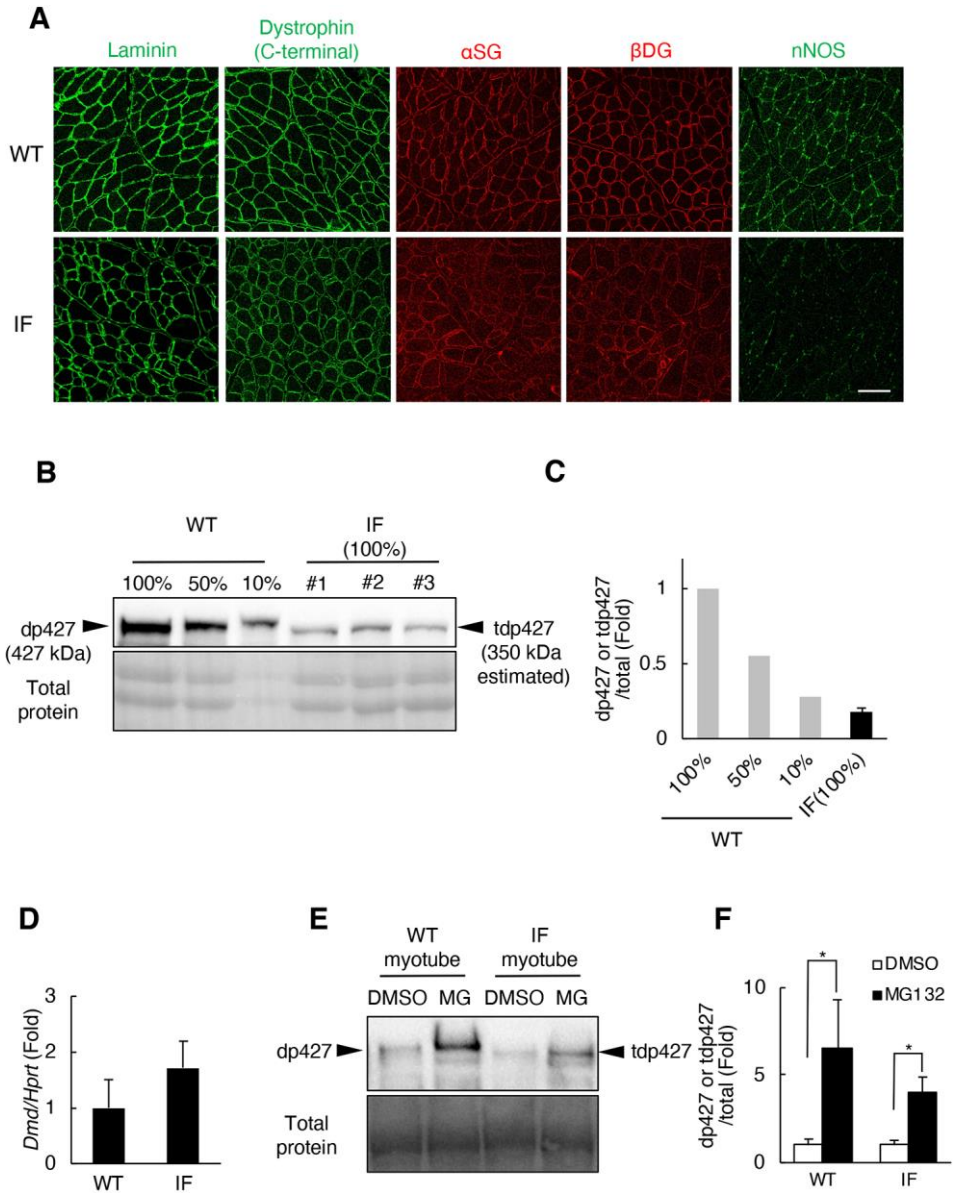

Fig. 4. Expression of truncated dystrophin and DGC components in the skeletal muscle of IF rats

(A) Immunohistochemical staining of laminin, dystrophin, and other DGC components in TA sections of 11-month-old WT and IF rats. Dystrophin was detected with rabbit monoclonal antibody ab154168. Scale bar = 50 μm.

(B) Immunoblot analysis of dp427/tdp427 protein expression in TA of 1-month-old WT rats at three dilutions, and of age-matched IF rats. Ponceau S staining was used as a loading

control.

(C) dp427/tdp427 expression levels quantified by the immunoblot analysis shown in figure 4B. Data are presented as means+SD (IF: n = 3)

(D) *Dmd* mRNA levels standardized by *Hprt* in TA of 1-month-old WT and IF rats. Data are presented as means+SD (WT: n = 3, IF: n = 6).

(E) The effect of proteasome inhibitor (MG132) treatment on the expression of dp427/tdp427 protein in myotubes derived from WT/IF skeletal muscles. Dystrophin was detected with rabbit monoclonal antibody ab154168. Ponceau S staining was used as a loading control.

(F) dp427/tdp427 expression levels quantified by immunoblot analysis shown in figure 4B. Data are presented as means+SD (IF: n = 3).

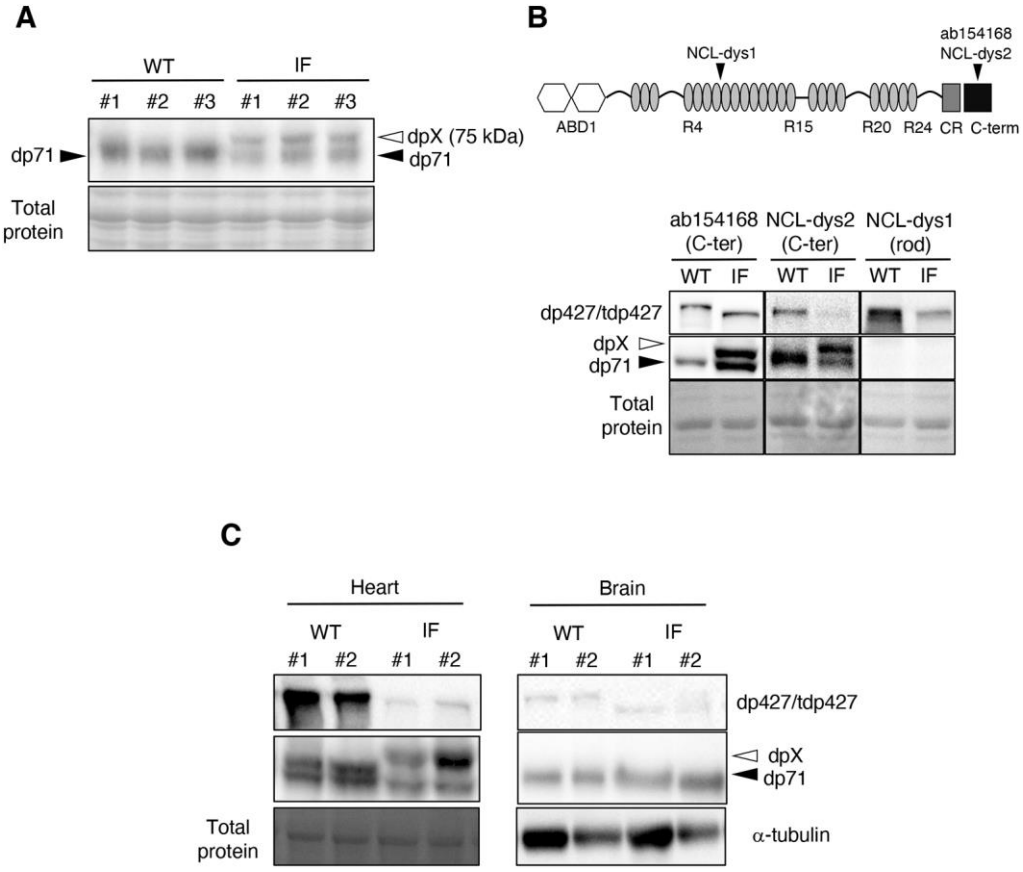

Fig. 5. Expression of additional dystrophin (dpX) in IF rats

(A) Immunoblot analysis on the lysates from TA of 1-month-old WT and IF rats. Ponceau S staining was used as a loading control.

(B) Comparative immunoblot analysis with different anti-dystrophin antibodies on the lysates from TA of 1-month-old WT and IF rats. The blots were analyzed with antibodies against the C-terminus (ab154168, NCL-dys2) and rod domain (NCL-dys1) of full-length-dystrophin. Ponceau S staining was used as a loading control. The upper figure stands for the composition of full-length dystrophin and the sites of the immunogen of three antibodies on it.

(C) Immunoblot analysis on the heart and brain lysates of 1-month-old WT and IF rats. Dystrophin detection was performed with anti-dystrophin antibody (ab154168). Ponceau S staining (heart) and α-tubulin (brain) were used as a loading control, respectively.

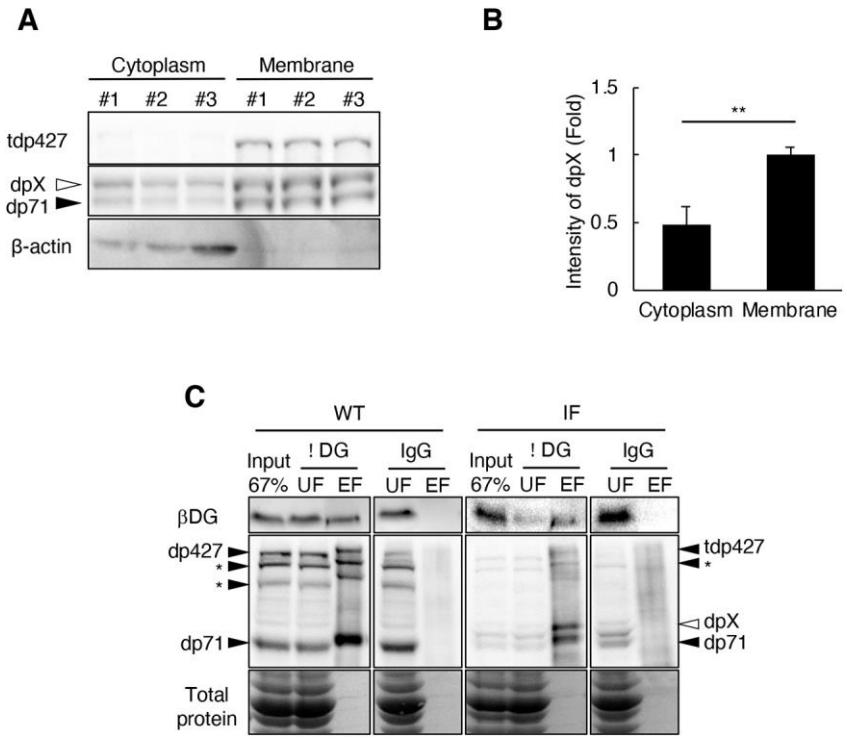

Fig. 6. Membrane-localization of dpX

(A) Immunoblot analysis with anti-dystrophin (ab154168) antibody on the cytoplasm and membrane fraction of skeletal muscles of IF rats. Equal amounts of protein were applied to each well. β-actin was used as a cytoplasm marker.

(B) Relative intensity of dpX in cytoplasm and membrane fraction shown in Figure 6A. Data are presented as means+SD (n = 3, in each group). $^{**}P < 0.01$, analysis using *t*-test.

(C) Immunoblot analyses on immunoprecipitated fractions with anti-βDG antibody (7D11) and with an isotype matched control antibody (IgG) as a control. The immunoprecipitation was performed on the membrane preparation from TA of 1-month-old WT and IF rats. The blots were analyzed with 7D11 and anti-dystrophin antibody (ab154168). UF: Unbound fraction, EF: elution fraction. Asterisks indicate unknown additional bands. Ponceau S staining was used as a loading control

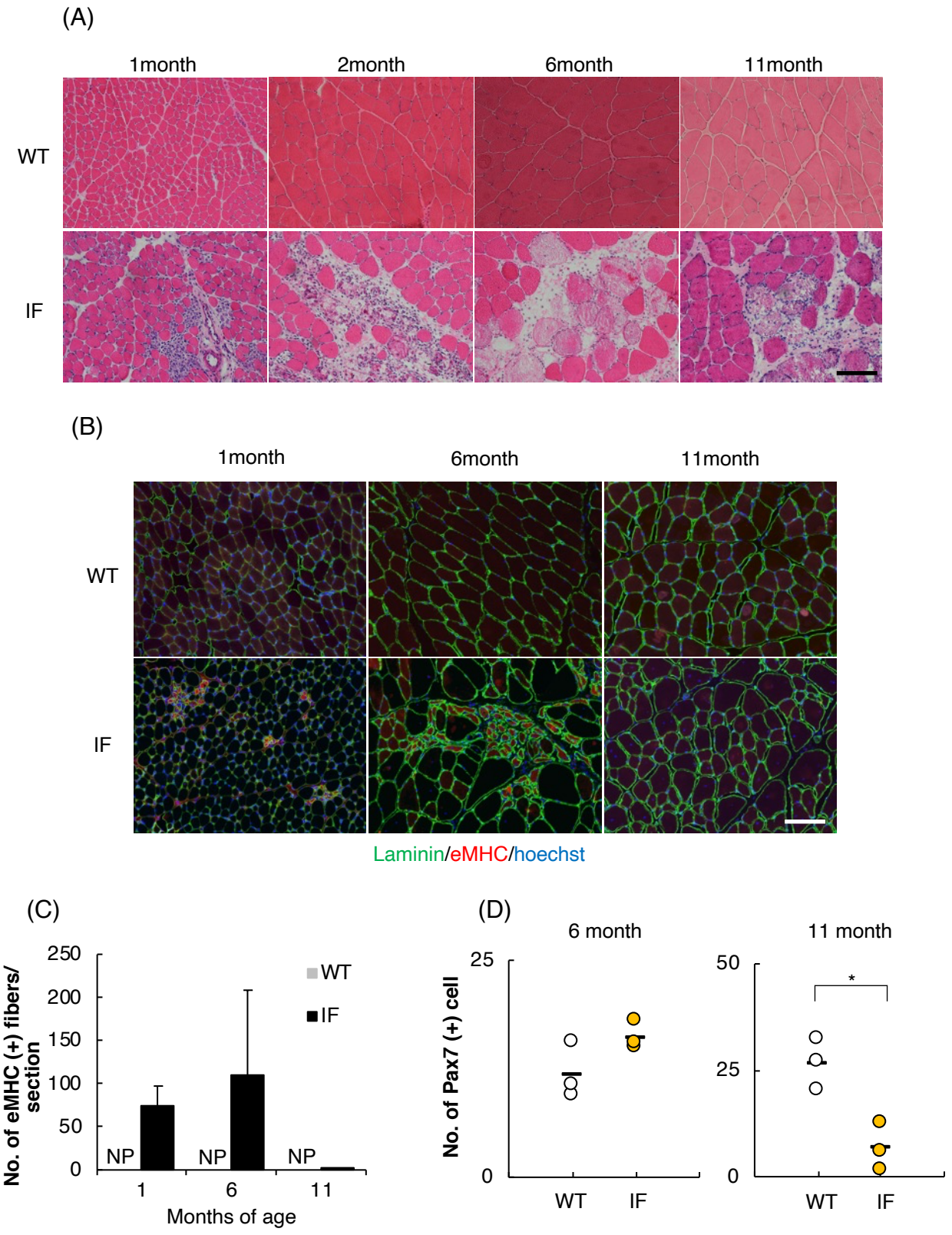

Figure. S1 Continuous degeneration and age-related change of regeneration capacity in skeletal muscles of IF rats.

(A) Representative images of H&E staining on TA muscle sections of 1, 2, 6, 11-month-old WT and IF rats. Scale bar = 50 μm.

(B) Representative images of immuno-staining for eMHC on TA muscle sections of 1, 6, 11-month-old WT and IF rats. Scale bar = 50 μm.

(C) The number of eMHC-positive fibers per TA section of 1, 6, 11-month-old WT and IF rats. Data are presented as means+SD (n=3-4, in each group). NP= not present.

(D) The number of Pax7(+) satellite cells per well on day 2 in primary culture from 6, 11-month-old WT and IF rats. Bars represent the mean value of each group. *P < 0.05, by t-test.

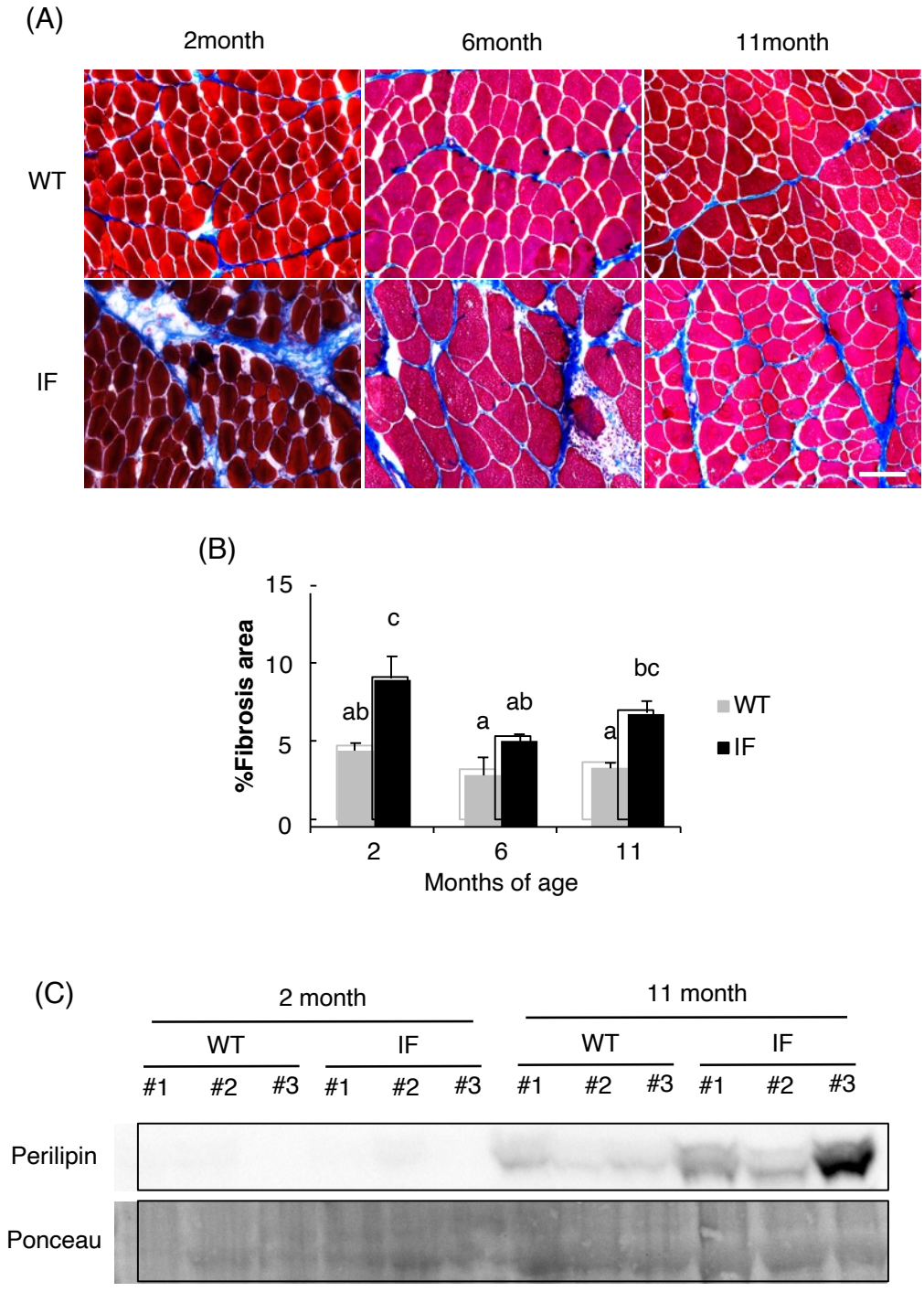

Figure. S2 Promoted fibrosis and accumulation of adipose tissues in skeletal muscles of IF rats.
(A) Representative images of Masson trichrome staining on TA muscle sections of 2, 6, 11-month-old WT and IF rats. Scale bar = 50 μm.
(B) Percentage of fibrosis area in total area observed in TA muscle sections of 2, 6, 11-month-old WT and IF rats. Different letters indicate significant differences between groups ($P<0.05$, by Tukey's test). Data are presented as means+SD (n=3, in each group).
(C) Immunoblot analysis of perilipin protein expression in TA of 2, 11-month-old WT and IF rats. Ponceau S staining was used as a loading control.

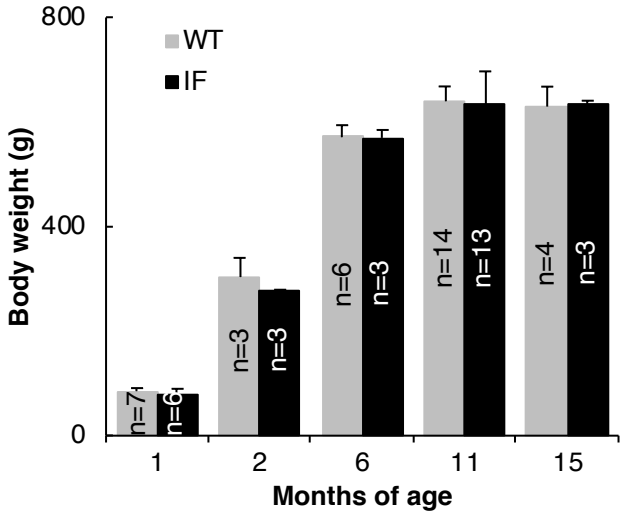

Figure. S3 Body weight of WT and IF rats
Body weight of 1, 2, 6, 11, 15-month old WT and IF rats. Data are presented as means+SD (n=3-14, in each group).

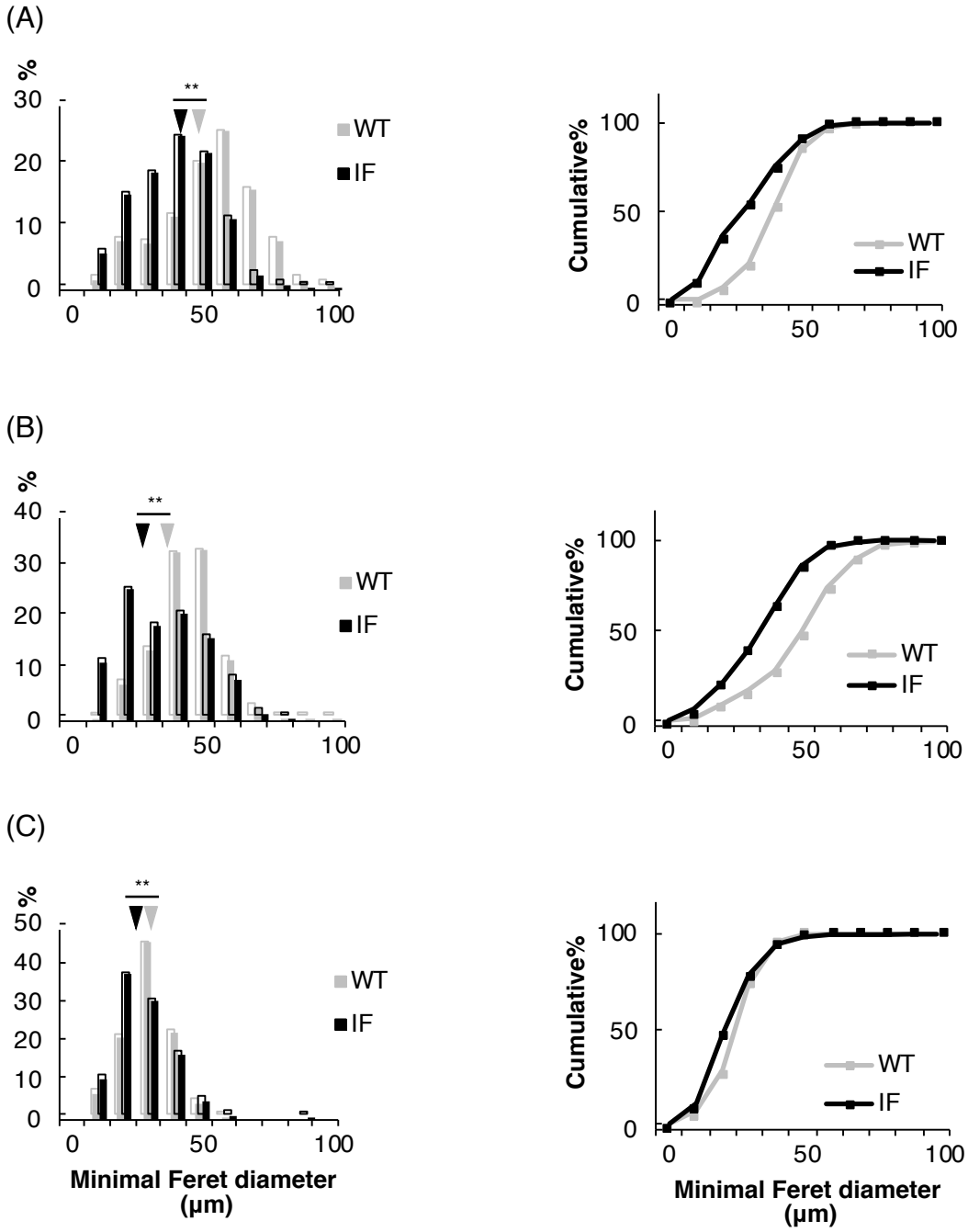

Figure. S4 IF soleus muscles have reduced myofiber size compared with WT.
Relative distributions and cumulative plots of myofiber size in SOL at 2- (A), 6- (B), and 11-month-old (C) WT and IF rats. Each arrowhead indicates a median value of each group. The data in each group contains the total number of detected myofibers from 3 subjects per group. $^{**}P < 0.01$, analysis using Wilcoxon rank sum test.

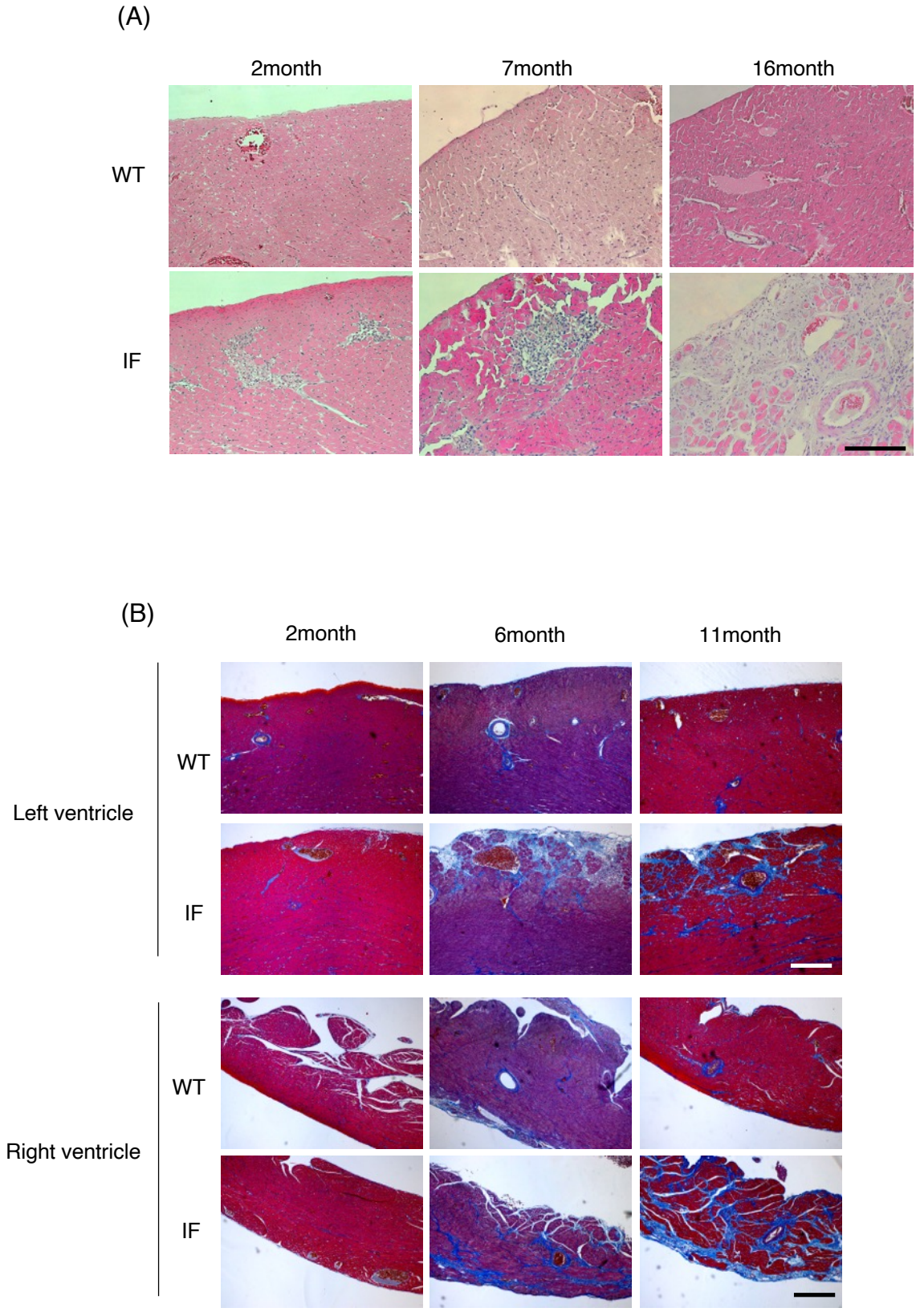

Figure. S5 Continuous degeneration and progression of fibrosis in cardiac muscles of IF rats.
(A) Representative images of H&E staining on left-ventricular-wall sections of 2, 7, 16-month-old WT and IF rats. Scale bar = 100 μm.
(B) Representative images of Masson trichrome staining on left- and right-ventricular-wall sections of 2, 6, 11-month-old WT and IF rats. Scale bar = 100 μm.

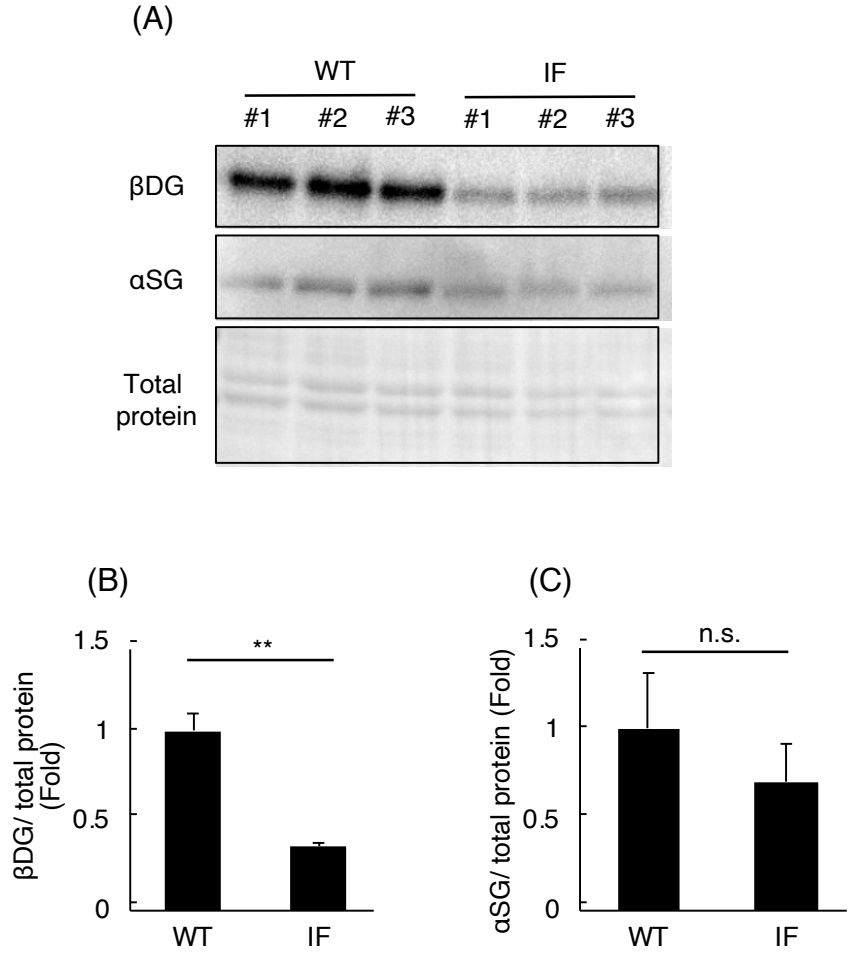

Figure. S6 Reduction of DGC components expression in skeletal muscle of IF rats.
(A) Immunoblot analysis of β-dystroglycan and α-sarcoglycan protein expression in TA of 1-month-old WT and IF rats. Ponceau S staining was used as loading control.
(B, C) β-dystroglycan (B) and α-sarcoglycan (C) expression levels quantified by the immunoblot analysis shown in figure S5A. Data are presented as means+SD (n=3). **P < 0.01, n.s.=not significant, by t-test.

Table S1. Other Echocardiographic Variables

Variables	7 month			16 month		
	WT (4)	IF (4)	P (t-test)	WT (5)	IF (5)	P (t-test)
Heart rate (bpm)	327 ± 18	354 ± 29	0.221	335 ± 19	332 ± 29	0.869
Left Heart Variables						
Septal wall thickness (mm)	1.7 ± 0.3	1.6 ± 0.4	0.769	1.7 ± 0.1	1.5 ± 0.3	0.315
Posterior wall thickness (mm)	1.9 ± 0.1	1.8 ± 0.1	0.363	1.8 ± 0.3	1.8 ± 0.2	0.774
LV end-diastolic diameter (mm)	9.5 ± 0.6	8.7 ± 0.4	0.12	10.1 ± 0.6	9.8 ± 0.4	0.492
LV end-systolic diameter (mm)	6.2 ± 0.7	5.1 ± 0.1	0.037	6.1 ± 1.3	5.8 ± 1.0	0.727
LV fractional shortening (%)	35.4 ± 3.8	42.0 ± 3.5	0.069	39.5 ± 11.7	40.7 ± 10.2	0.888
Transmitral E velocity (cm/s)	110 ± 23	126 ± 7	0.281	118 ± 19	104 ± 18	0.344
Transmitral E deceleration time (ms)	53 ± 16	42 ± 4	0.302	39 ± 8	49 ± 11	0.164
LV myocardial performance index	0.33 ± 0.05	0.26 ± 0.06	0.194	0.27 ± 0.04	0.33 ± 0.13	0.351
Sm septum (cm/s)	3.8 ± 0.7	4.2 ± 1.1	0.685	3.4 ± 0.3	4.0 ± 0.5	0.085
Sm lateral (cm/s)	6.1 ± 0.9	5.2 ± 1.0	0.296	5.9 ± 0.7	4.5 ± 0.7	0.021
Ea septum (cm/s)	6.9 ± 2.8	5.9 ± 2.0	0.640	6.4 ± 0.5	5.0 ± 1.5	0.149
Ea lateral (cm/s)	6.3 ± 1.7	6.1 ± 2.3	0.912	5.7 ± 1.5	4.7 ± 0.9	0.305
Transmitral E/Ea septum	18.8 ± 8.2	23.5 ± 6.5	0.465	18.6 ± 4.6	22.2 ± 5.5	0.383
Transmitral E/Ea lateral	18.4 ± 4.5	22.7 ± 5.7	0.342	22.2 ± 6.3	23.1 ± 5.9	0.833
Right Heart Variables						
RV fractional area change (%)	41.5 ± 3.7	44.0 ± 3.8	0.457	41.3 ± 6.1	39.5 ± 6.5	0.683
TAPSE (mm)	1.8 ± 0.5	2.3 ± 0.3	0.189	2.3 ± 0.3	1.5 ± 0.6	0.061
Transtricuspid E velocity (cm/s)	67.2 ± 19.8	77.1 ± 12.3	0.191	84.7 ± 5.4	72.2 ± 18	0.666
Sm RV free-wall (cm/s)	5.6 ± 0.4	5.1 ± 0.3	0.096	4.6 ± 0.7	3.9 ± 0.9	0.279
Ea RV free-wall (cm/s)	7.9 ± 2.2	5.5 ± 1.5	0.425	9.1 ± 0.7	6.1 ± 3.4	0.357
Transtricuspid E/Ea RV free-wall	9.0 ± 2.8	15 ± 4.9	0.842	9.4 ± 1.1	12.3 ± 6.4	0.525
Maximum IVC diameter (mm)	3.6 ± 1.0	2.6 ± 0.4	0.161	3.1 ± 0.8	3.0 ± 0.3	0.849

Table S1 Values from echocardiography
*P<0.05, WT vs age-matched IF, by t-test. Numbers in parentheses represent the number of subject in each group.

Table S2 List of primers

		Forward	Reverse
Fig. 1C	genome #1	5'-AAAAGGAGAACAGGAGTTTTTGAAT-3'	5'-TACAGTAGCTGAGTCAATGAGGTTG-3'
	genome #2	5'-GAATACCTTTGGGTGTGACTGTATC-3'	5'-TACAGTTTTCCATTTCTGAAGAACC-3'
Fig. 1D	mRNA #1	5'-AAAGCAACACATAGACAACCTCTTC-3'	5'-CCTCTTGGGCATGTTTTACCA-3'
	mRNA #2	5'-GAACTCAGCTCTTGAAGGCAAT-3'	5'-CTTCCAAAGTTTTGCATTTTCC-3'
Fig. 4D	*Dmd*	5'-GGAAGATCTGAATACCAGATGGA-3'	5'-CTGCCTGACACGGTCCTC-3'
	Hprt	5'-GACCGGTTCTGTCATGTCG-3'	5'-ACCTGGTTCATCATCACTAATCAC-3'